Chemical Engineering Journal 450 (2022) 137999

Contents lists available at ScienceDirect

Chemical Engineering Journal

journal homepage: www.elsevier.com/locate/cej

# Effect of free radicals and electric field on preparation of coal pitch-derived graphene using flash Joule heating

Pengfei Huang [a], Rongtao Zhu [a,b,*], Xinxi Zhang [a,b,*], Wenjun Zhang [b]

[a] Key Laboratory of Coal Processing and Efficient Utilization of Ministry of Education, China University of Mining and Technology, Xuzhou 221116, Jiangsu, China
[b] School of Chemical Engineering and Technology, China University of Mining and Technology, Xuzhou 221116, Jiangsu, China

ARTICLE INFO

*Keywords:*
Flash Joule heating
Coal pitch
Free radicals
Graphene
Electric fields

ABSTRACT

Most of the traditional graphene production processes were not only solvent-intensive but also time-and-energy-consuming. Flash Joule heating (FJH) is an efficient approach to green and scalable large-scale production of graphene. However, its reaction mechanism is not clear during the process of electric field and free radical on graphene generation. In this work, synthesis of coal pitch-based graphene by FJH under the coupling effect of temperature and electric field, and Raman spectroscopy and electron transient magnetic resonance were studied at different input energies. The results show that the input energy is positively correlated with the generated radicals and is beneficial for the quality improvement of graphene. In addition, the mechanism is explained using ReaxFF molecular dynamics and DFT calculations: Joule heat provides energy for the kinetics and thermodynamics of the reaction. High temperature (3000 K) can dissociate branch chains in coal tar molecules to generate highly reactive alkane and alkene radicals. Different cooling rates affect the quality of graphene generation. When the cooling rate is slow, the graphite microplates will grow in layers, and a multi-layer phenomenon will appear; when the cooling rate is fast, the generated graphene will be in a turbostratic order. At the same time, the DFT calculation shows that the coal tar molecules are ionized under the action of the electric field and are oriented and arranged to reduce the reaction potential barrier.

## 1. Introduction

Most of the traditional graphene production processes [1,2] are solvent-intensive, and time-and-energy-consuming. The corresponding high production costs are not conducive to large-scale industrial applications, including micromechanical exfoliation [3,4], reduced graphene oxide[5,6], chemical vapor deposition[7], and epitaxial growth[8]. Moreover, the various excellent properties of graphene can only be displayed when the quality of graphene is high. With the increase of the number of layers and the accumulation of internal defects, the superior properties of graphene will be reduced[9,10]. Most bulk graphene is produced by the top-down method of exfoliating graphite, which usually requires a large amount of solvents for high-energy mixing, shearing, ultrasonic or electrochemical treatment[11,12]. These AB-stacked graphene layers have a highly ordered arrangement between them[13]. Although the chemical oxidation of graphite to graphene oxide promotes exfoliation, it requires harsh oxidizing agents and leaves graphene with defective perforated structures in the subsequent reduction step [14,15]. If chemical vapor deposition or advanced organic methods are used, bottom-up synthesis of high-quality graphene would be usually limited to ultra-small amounts[16,17]. Therefore, the synthesis process of graphene and other materials needs to be improved.Table 1..

It has been found that the flash Joule heating (FJH) of many cheap carbon sources (such as coal, petroleum coke, biochar, carbon black, waste food, rubber tires, and mixed plastic waste) can produce graphene in less than 1 s, and the graphene produced is called “Flash Graphene” (FG) [18–22]. The process does not use a furnace, solvent or reaction gas, and the yield depends on the carbon content of the source; if a high carbon source is used, the yield can even reach 80% to 90%, and the carbon purity is greater than 99%[23,24]. The unique turbine layered structure of FG allows it to maintain the optical and electronic properties of two-dimensional graphene even when hundreds of graphene layers are stacked[23].

However, FJH is a very short reaction time due to its use of the material’s own electrical resistance exotherm under the action of an electric field. And it is the coupling of electric field and temperature field

* Corresponding authors at: Key Laboratory of Coal Processing and Efficient Utilization of Ministry of Education, China University of Mining and Technology, Xuzhou 221116, Jiangsu, China.
*E-mail addresses:* rtzhu2010@cumt.edu.cn (R. Zhu), zhangxinxi@cumt.edu.cn (X. Zhang).

https://doi.org/10.1016/j.cej.2022.137999
Received 9 May 2022; Received in revised form 3 July 2022; Accepted 6 July 2022
Available online 9 July 2022

**Table 1**
Parameters of finite element simulation.

| | $\sigma$/ S/m | $C_p$/ J/(kg*K) | $\varepsilon_r$ | $\rho$/ kg/m$^3$ | $k$/ W/(m*K) |
|---|---|---|---|---|---|
| **Electrodes** | 5.998e7 | 385 | 1 | 8940 | 400 |
| **Sample** | 600 | 710 | 1 | 1950 | 150 |
| **Quartz** | 1e-14 | 730 | 4.2 | 2210 | 1.4 |

together, unlike the general pyrolysis by the action of single temperature field. Due to the complexity of the FJH process, the detailed mechanism is still a question that has not been fully investigated so far. Reactive molecular dynamics (ReaxFF) could provide new insights into the microscopic nature of the thermal transformation of carbon materials and become a more suitable alternative approach to elucidate the intrinsic reaction mechanism[25].

Usually, carbon-based materials produced by thermal processes contain large amounts of Persistent Free Radicals (PFRs), and the breakage of chemical bonds in the precursors may be the main reason for the formation of PFRs[26]. The formation of PFRs in carbon-based materials produced by other methods has been reported, such as chemical vapor deposition[27], laser ablation[28] and arc discharge methods[29]. Experimental studies on radicals as key elements in carbon aggregation and particle formation of graphene are necessary. Electron paramagnetic resonance (EPR) spectroscopy has long provided valuable probes of the radical sites and electronic properties of carbon-based materials[30]. In this case, the spectral features of EPR reflect the influence of the chemical environment on the magnetic properties of unpaired electrons, making it a particularly useful probe for studying π-conjugated carbon in FJH processes[31].

In this study, coal-based graphene was prepared by flashing Joule heating based on capacitor discharge. Then, at the high temperature of over 3000 K the graphitization of coal pitch was realized, and the ultra-fast cooling rate avoided the AB stacking of aromatic sheets. More importantly, compared with traditional preparation methods, the preparation of graphene could be realized more quickly and economically. At the same time, by using EPR and Raman spectroscopy, this study further explored the relationship between the size, number of layers, defect density, free radical concentration and input energy of the FG. Finally, the mechanism of action of the FJH is explained in terms of the molecular dynamics of the reaction and DFT calculations.

## 2. Experiment

### 2.1. 1 Materials and methods

The circuit diagram of the FJH system was shown in a previously published work[32]. As is shown, the system is composed of a control module, a charging module, a discharging module, a workpiece module, an energy storage module, a measurement module, and a sample stage. The raw materials were treated as follows: before using FJH, coal pitch (CP) (Hebei Province, China) was broken into powder by a crusher, and the powder smaller than 200-mesh (0.074 mm) was screened out for the next FJH. Then 120 mg of crushed CP (200 mesh) was accurately weighed with an analytical balance and placed into a quartz tube (length 50 mm, inner diameter 6 mm, wall thickness 2 mm), and the two end surfaces were sealed with graphite blocks, the sample resistance was controlled at 0.5 Ω by applying a certain force to the sample. Since the gap between the graphite block and the quartz tube influenced the sealing performance poorly, a layer of conductive copper tape was attached to the graphite block to prevent the broken CP powder from escaping. Finally, CP was processed with FJH system, and then named as FG. The FJH device used in this experiment had a capacitor bank with a capacitance of 60 mF and a voltage of 0–450 V. The discharge time was set to 1 s so that the electricity in the capacitor could be completely discharged, when the discharge time was not specified. In such a short time, the reaction temperature reached an ultra-high level (greater than3000 K) immediately, and the heating/cooling rate was $10^5$ K $s^{-1}$.

### 2.2. Material characterization

The morphology and microstructure of CP and FG were studied by SEM (MAIA3 LMH, USA). X-ray powder diffraction (XRD) was conducted using a Bruker D-8 Advance diffractometer (USA) with nickel-filtered Cu Kα (λ = 1.54178 Å) radiation at room temperature and the data was collected from 5° to 80° with a scan rate of 2° $min^{-1}$ to obtain phase structure of CP and FG. Raman measurements were done for the composite by a Raman spectrometer (Senterra, Bruker, Germany) equipped with a 532 nm laser line to determine the chemical composition and structure of CP and FG.

A precision balance (SARTRIUS, CP225D) was used to weigh 5.00 mg of the sample. The X-band (9 GHz) of the Electron Paramagnetic Resonance Spectrometer (JES-FA200, JEOL, Japan) was used for testing. The specific parameters were as follows: microwave power 0.998mW, central magnetic field 321.569mT, sweep width 10mT, modulation width 0.8mT, time constant 0.03 s, sweep time 30 s, magnification 80, and frequency 9036.107 MHz.

### 2.3. Electrochemical measurement

The 0.5 mm thick nickel mesh was cut into pieces with a size of 1 cm × 2 cm, which were then ultrasonically cleaned with absolute ethanol and acetone for 10 min in turn. After that, they were dried in a vacuum drying oven, and weighed its mass $m_1$ (mg) after drying. The sample, carbon black and binder PTFE were weighed in a mass ratio of 8:1:1 to make a slurry, which was coated evenly on the current collector. The coated sample was dried in a vacuum drying oven, pressed into tablets, and weighed as $m_2$ (mg). The mass of the active substance attached to the current collector was calculated by formula (2–1) and recorded as Δm (mg).

$$\Delta m = (m_2 - m_1) \times 0.8 \quad (1)$$

The electrochemical analyzer was used to test the electrochemical capacitance performance of the sample, including cyclic voltammetry (CV curve) and impedance spectroscopy (Nyquist spectrum). The test system was a three-electrode. The calomel electrode (Hg / HgO) was selected for the reference electrode based on the alkalinity. The electrolyte used was a 6 mol·$L^{-1}$ KOH solution.

The electrochemical performance was evaluated by using electrochemical workstation (Wuhan Corrtest Instruments Corp., Ltd, China, CS660). The electrolyte was a 6 M KOH solution, as well as Ag/AgCl and a platinum sheet was used as the reference electrode and the counter electrode, respectively. Subsequently, the charge and discharge measurement of the electrode was a constant current test in the range of 0.001–1 V vs. Ag/AgCl at room temperature, and the cyclic voltammetry (CV) and electrochemical impedance spectroscopy (EIS) measurements were performed on an electrochemical workstation. CV was performed at a scan rate of 0.01–0.1 mV $s^{-1}$ and EIS was collected by applying a sine wave with an amplitude of 10.0 mV.

### 2.4. Finite element simulation

The structure of the flash graphene model is as follows: the yellow ones at the top and bottom are copper electrodes with length of 5 mm and diameter of 6 mm; the black one in the middle is the sample with length of 5 mm and diameter of 6 mm; the thickness and length of the outer quartz tube are 1 mm and 15 mm, respectively. the initial temperature of all materials is 293.15 K[33].

The relevant properties of the materials are shown in the following table.

### 2.5. Computational details

The theoretical calculation of mapping the electrostatic potential of the sample was conducted by using the Dmol 3 program. All calculations were performed using standard gradient techniques and default convergence criteria. Molecular dynamics simulations were performed using the LAMMPS package and interactions between C, O, and H atoms were described using the ReaxFF force field. The three directions of the system are set as periodic boundary conditions, the system is calculated using a canonical ensemble (NVT), and the simulation time is 1500 ps.

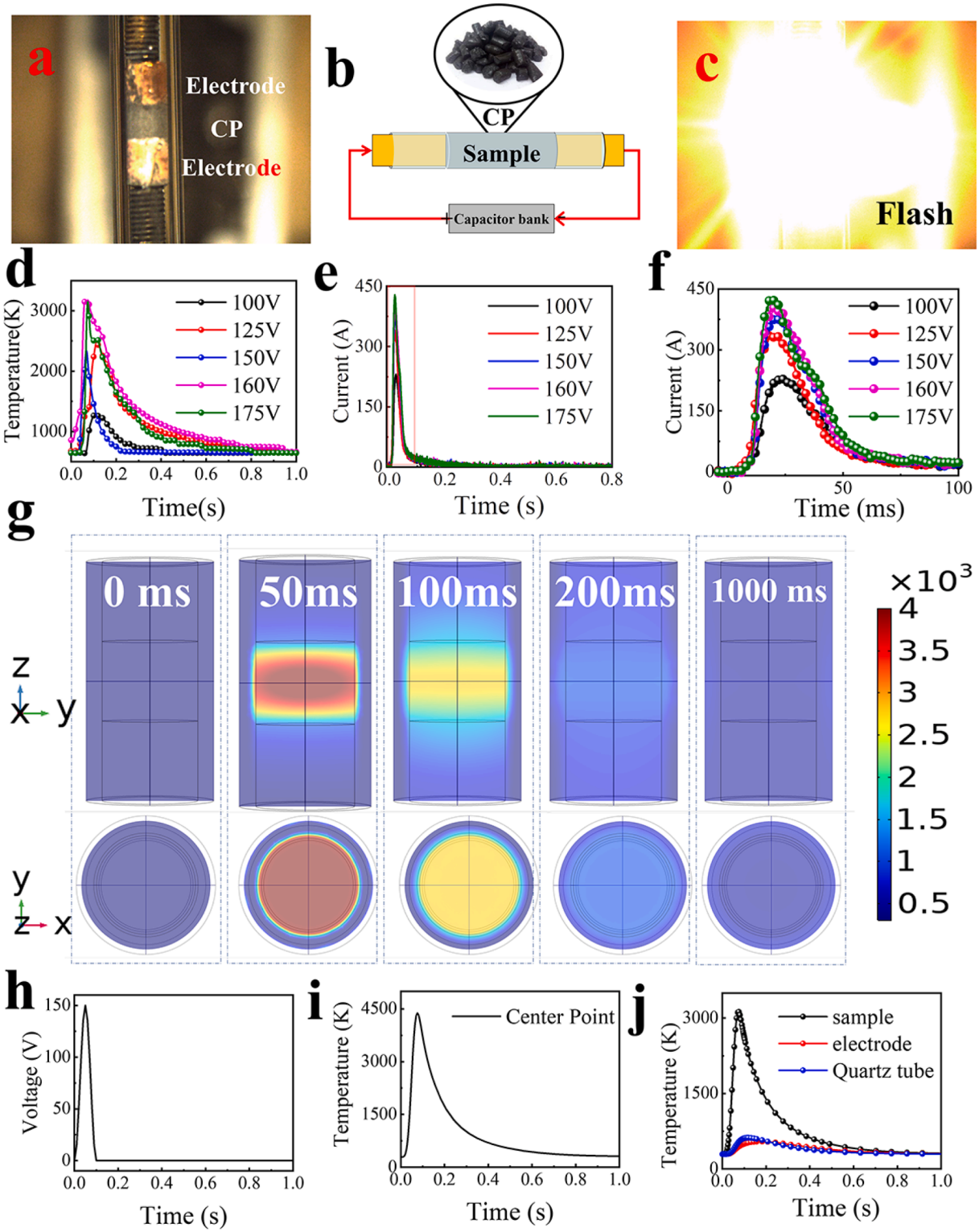


**Fig. 1.** (a) optical photograph of the FJH sample; (b) Schematic diagram of the FJH device; (c) snapshot of the FJH during discharge; (d) curves of current versus time at different FJH voltages; (e) local magnification of the current; (f) curves of temperature versus time at different FJH voltages; (g) temperature clouds for different times of the FJH process obtained using COMSOL simulation; (h) voltage profile imposed by COMSOL simulations; (i) the curve of the temperature of the sample center point during the COMSOL simulation; (j) the curve of the average temperature of the sample, electrode and quartz tube by COMSOL simulation.

## 3. Results and discussion

### 3.1. The influence of process parameters

In order to synthesize FG, coal pitch (CP) is enclosed in a quartz tube and pressed between two copper electrodes. The graphite block is in physical contact with the CP, as shown in Fig. 1(a). The electrodes are connected to a capacitor bank with a total capacitance of 60 mF and charged to a voltage of 160 V. The schematic diagram of the FJH system can be seen in Fig. 1(b), and flashing phenomenon can be observed in Fig. 1(c). The capacitor bank generates FJH by discharging the CP, which quickly heats the CP to about 3000 K (Fig. 1(d)) in a few hundred milliseconds, and then cools to room temperature in a few seconds. By adjusting the pulse voltage, the peak current (Fig. 1 (b)) and total energy passing through the sample will be changed. A pulse current of about 100 ms was observed during its discharge in Fig. 1(e), which is consistent with the heating curve, and its peak current increased rapidly with the increase of the initial voltage. The duration of its flash is the longest at 160 V, as can also be seen from the high-speed camera shot in Fig. S1. As the initial voltage increases, the amount of energy released is increasing rapidly (Fig. S2(a)). But when the voltage reaches 160 V, the end voltage rises rapidly. This is because when the voltage is greater than 160 V, the Joule heat it receives reaches the threshold, the aliphatic in the coal pitch decomposes and releases a lot of gas, and the resistance of the sample increases accordingly. Ultimately, the open circuit causes the flash time to be shorter at 175 V than at 160 V. As shown in Fig. 1(f), the resistance change is also reflected in the current change. When the voltage is lower than 160 V, the smooth current curve proves that the change is uniform. When the voltage is greater than 160 V, a significant slowdown in 40 ms, which can also be further proved by the change in time with the termination voltage in Fig. S2(a). The circuit is disconnected, so its end voltage rises rapidly, and the joule heat received by it also decreases, so the later experimental voltages are set at 160 V. Fig. S2 (b) shows the energy and voltage change at different times under 160 V voltage. It can be seen that as the energization time increases, the voltage change first significantly decreases, and the energy release increases first and then stabilizes. At 100 ms, about 700 J of energy is released, amounting for 91% of the total energy stored.

The finite element simulation of the FJH process was carried out using the electrothermal coupling and solid heat transfer of COMSOL software, and the joule heat generation and transfer process were analyzed in detail. Fig. 1(h) shows a typical FJH process, where a pulse potential with a duration of 100 ms and a peak value of 150 V is applied to the electrode, and the other electrode is grounded. It can be seen from Fig. 1(g) that the center of the sample is the region with the highest temperature, and the temperature in the XY direction of the sample is relatively uniform. The midpoint temperature rises first, and then the heat spreads to both ends. It is worth noting that the midpoint temperature of the sample is significantly higher than the junction point of the electrode and the sample. Fig. 1(i) is the curve of the sample temperature at the center point changing with time, the sample heats up rapidly under the action of the pulse current, and the temperature reaches its peak value within 100 ms. The heating rate reaches$3 \sim 5 \times 10^5 K/s$, and the cooling rate reaches$10^4 K/s$. Meanwhile, Fig. 1(j) shows that the average temperature of the electrode and the quartz tube is less than 500 ℃ during the finite element simulation, and the temperature drops to room temperature within one second, which is consistent with the experimentally observed results. All these results show that extremely pure graphene can be generated by FJH process of capacitive pulse discharge[20], it can bring the average temperature of the carbonaceous material above 3,000 K, and the midpoint temperature exceeding 4,000 K locally to volatilize non-carbon elements in the sample.

### 3.2. Typical morphology and structure

A typical coal pitch sample was observed by SEM. The material is composed of graphitized carbon and amorphous carbon particles (Fig. 2 (a)). After the FJH, the amorphous carbon on the surface of the sample is transformed into graphite nanosheets (Fig. 2 (b)). TEM analysis can further observe that the lattice spacing of FG is increased by 3.71 Å, which is significantly larger than the 3.34 Å spacing observed in AB graphite in Fig. 2 (c). The presence of Moiré patterns as well as selected area electron diffraction (SAED) patterns[20] showing four different sets of six-membered ring mismatches at 21° were observed by TEM images. This rotational orientation can also be confirmed optically, reducing van der Waals interactions and making FG easier to disperse. Fig. 2 (f-g) shows the XPS characterization results before and after FJH. It can be seen from the full spectrum that that the oxygen peak of the sample disappears and the carbon content increases after FJH, indicating that the elemental purity of the carbon can be achieved during the FJH process in Fig. 2 (f). Furthermore, the C peak can be divided into peaks at 284.8 and 285.7 eV, corresponding to sp2C and sp3C in the material, respectively. The peaks corresponding to the sp2 component are also enhanced in FJH, and the half-width (FWHM) changes from 0.87 eV to 0.73 eV (Fig. 2 (g)). It also can be seen from the XRD pattern of Fig. 2(h) that the original coal pitch sample has a sharp (0 0 2) characteristic peak, which proves that the original sample is stacked by multiple layers of graphite crystals. Combined with the analysis of the Raman spectrum in Fig. 3, it can be seen that the sample flakes after FJH by a few layers of stacked lamella structure. The results showed that the non-carbon elements were volatilized during the FJH process, and the carbon elements were purified and FG was generated.

### 3.3. The influence of parameters on FG

Raman spectroscopy is an important tool for analyzing the quality of graphene. Next, the graphitization degree and the number of lamellae of the sample by FJH are discussed in depth through the characterization of Raman spectroscopy. Fig. 3 (a-b) is the Raman spectra at different voltages and times. As shown in Fig. 3(c), there are at least five peaks with different strengths within the range of 1000 ~ 1800 cm, including the G peak of an ordered structure and the D, D1, D2, and D3 peaks of the disordered structure. With the increase of FJH voltage and time, the increase of graphitization degree causes the spectral peaks of D and D1 to decrease significantly after the structure is ordered, and the disordered structure peaks of D2 and D3 gradually disappear.

According to previous studies, the defect density $n_D$ after processing can be obtained by [34]:$n_D(\mathrm{cm}^{-1}) = (7.3 \pm 2.2) \times 10^9 E_L^4 (I_D/I_G)$, where $E_L$ is the Raman laser energy (5mW in this study), $I_D$ is the intensity of the D peak, $I_G$ is the intensity of the G peak. It is proved that during the FJH process, the size of sp2 clusters gradually increases, the defect density of the sample decreases, and the defect type changes from the disordered lattice structure such as amorphous, polyene vacancy and hybrid structure to the graphite sheet edge. The results of EPR are mutually confirmed. The density of defects and the change in grain size caused by defects have a non-negligible effect on the mechanical, electrical and optical properties of graphene. Raman spectroscopy can also be used to obtain the crystallite basal plane size of carbon materials. The principle is based on the reciprocal relationship between the graphitization degree obtained by Raman spectroscopy and the graphite crystallite size $L$ (mm) obtained by XRD [35].

$$L_a = \frac{4.4}{I_D/I_G} \tag{2}$$

Equation (2) shows that the sample grain size is inversely proportional to $I_D/I_G$. Compared with the original sample, the processed sample grain size and graphitization degree both increase. The size of sp2 clusters in the original sample is about 4.5 nm, and the size of the crystal

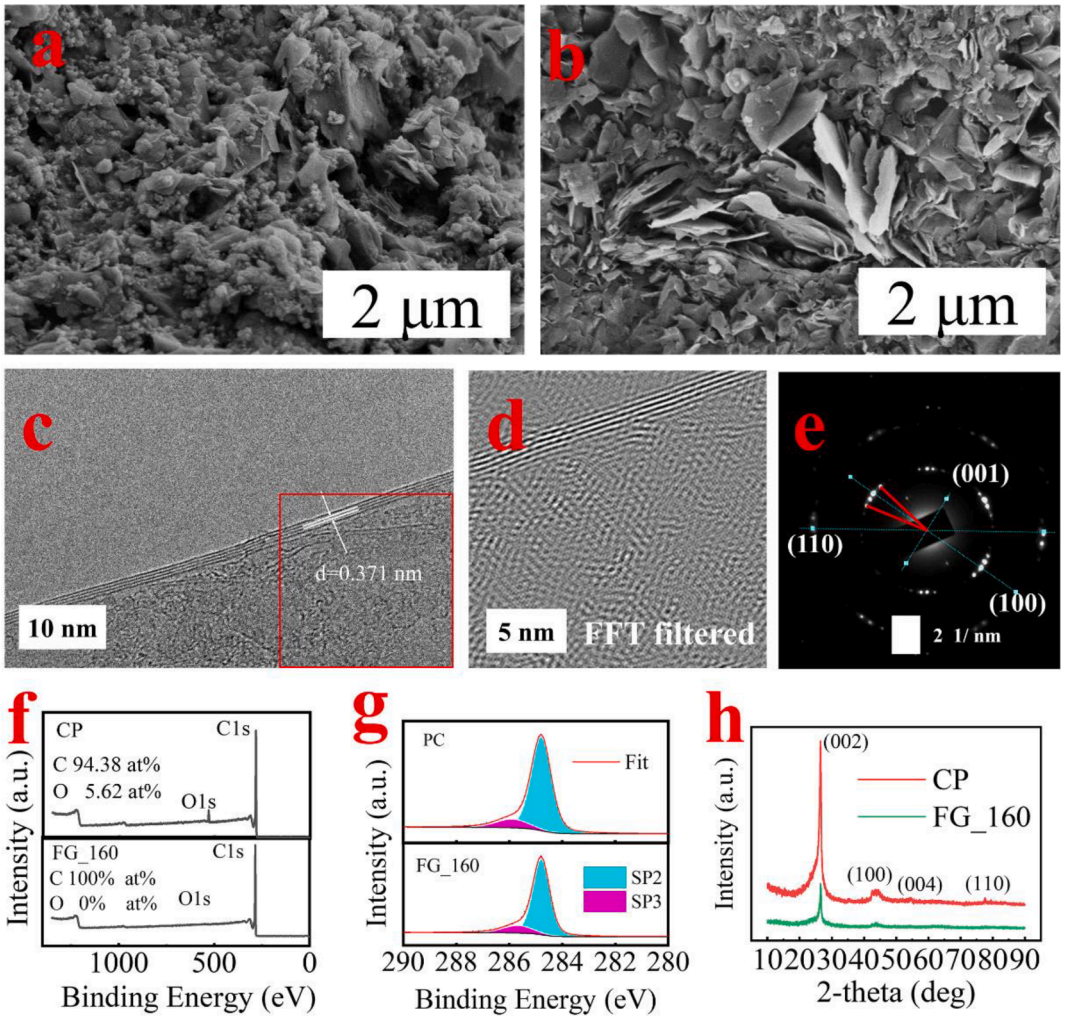


**Fig. 2.** SEM image of CP (a) and FG at 160 V (b); (c)TEM of FG at 160 V and the position for SAED (f) XPS of CP and FG at 160 V; (g) C1s spectra of CP and FG at 160 V; (h) XRD of the CP and FG at 160 V.

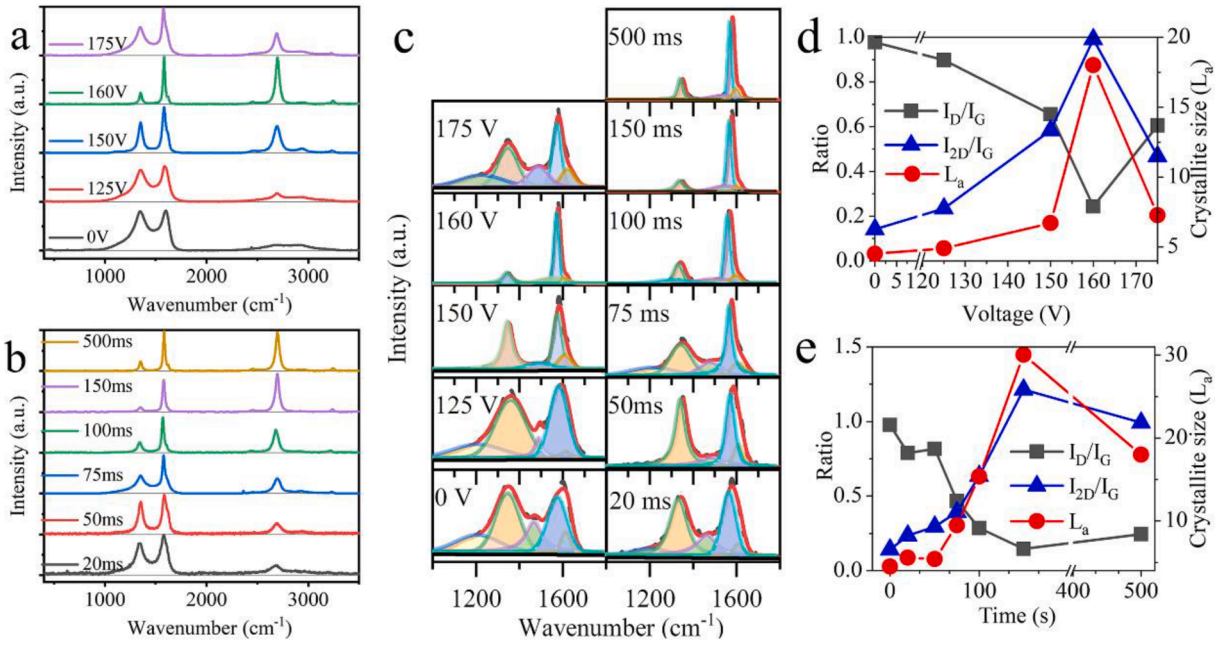


**Fig. 3.** (a, b) Raman spectra at different voltages and times; (c) peak fitting curve of raman spectrum; $I_D/I_G$, $I_{2D}/I_G$ and La changes with voltage (d) and time (e).

grains gradually increases with the increase of flashing time, and La rises to 30.0 nm at 150 ms. However, when the time reaches up to 500 ms, the grain size decreases. During the FJH process, the aliphatic hydrocarbons and amorphous carbon in the sample undergo depolymerization and condensation under the action of high-temperature joule heating. Then, the size increases, the lamella decreases, and a large number of irregular edge structures are formed. The sp3 hybrid space structure in the CP is destroyed, forming a large number of ordered sp2 components, and the CP are further exfoliated from the large graphite structure into a graphene structure under the FJH. Corresponding to the conversion of defects and edge structure, combined with the results of EPR, the free radical concentration of the sample displays a rising trend after FJH. It can be inferred that FJH will promote the graphitization of the sample, reduce flakes and increase the free radical concentration.

In order to compare the unpaired electron density of coal pitch samples treated with different voltages, the EPR spectrum intensity was quantified by measuring the area under the absorption curve (obtained from double integration). It can be seen from Fig. 4(a) show that the EPR signal has a narrower line width of the CP treated with a voltage at 125 V, which is a characteristic of local spin. It is derived from the local free radicals in the non-π-bonded electronic state, which is likely to be present in the sample. For the high graphitization levels of 150, 160, 175, and 200 V, compared with other samples, the basal plane of graphite remains more complete. Therefore, there are many delocalized π-electron radicals on their surface; most of the sp3 region is converted to sp2; and the graphitization degree is increased, which broadens the line width of their EPR signal. The free radical information obtained by ESR measurement is confined to long-lived (stable) free radicals, because when the sample is cooled to room temperature, active transient free radicals with poor stability disappear[36]. The unpaired carbon atoms on the carbon atoms (except those electrons on the edges and defects) are scattered along the carbon surface and exhibit rapid spin–lattice relaxation through the interaction with adjacent π electrons, which produces a large line width in EPR signal.

The free radicals of the samples used in this study were calibrated by the Mn standard. Fig. 4(b) shows the comparison of the free radical concentration under different voltages. It can be found that the free radical concentration is not high when the voltage is below 125 V, indicating that the energy of the voltage is insufficient to cause the covalent bond to break. When the voltage reaches above 150 V, a broad radical peak can be seen, and its radical concentration increases significantly. Interestingly, higher voltage does not guarantee higher free radical content. This is because when the voltage is 175 V, the sample will thermally expand, causing the input energy to be cut off. The content of free radicals is proportional to the input energy. Therefore, 160 V is an optimal choice to obtain a higher concentration of free radicals. Fig. 4(d) shows that changing the flash time of the sample under a voltage of 160 V can further adjust its free radical concentration. At 100 ms, the free radical concentration of the sample remains stable after reaching the peak as show in Fig. 4 (e). Therefore, it can be concluded that the free radical content of the sample can be gradually adjusted and optimized by changing the flash discharge time under a suitable voltage (160 V).

Fig. 4(c, f) can be obtained by choosing the input energy as the independent variable without the voltage and time alone. It can be seen that the grain size of the aromatic layer, the thickness of the lamella, the concentration of free radicals and the input energy are positively correlated, while the defect density is negatively correlated with the input energy. This is due to the high degree of ordering of the aromatic layer in coal pitch, which is not conducive to the re-bonding of unpaired electrons, resulting in a low concentration of free radicals. Under the action of the strong electric field and temperature field in the flashing process, the graphitization of the carbon leads to a decrease in defect density and an increase in the size of the aromatic layer. Due to the extremely short cooling time, the aromatic layer is too late for the AB stack to weaken its orientation, resulting in the generation of a large number of unpaired electrons and an increase in the concentration of free radicals.

### 3.4. Mechanism explanation

Density functional theory (DFT) calculations were also carried out to further explore the influence of the external directional electric field on the electronic state of carbon atoms in the CP model. The molecular electrostatic potential (MEP) maps in Fig. 5(a)is maps the electrostatic potential of the molecule to the total electron density surface, the blue areas on the MEP are positively charged and the red areas are negatively charged. At zero electric field (Fig. 5(a_0)), the difference in electron charge density at its edges and at its center is negligible. Then, under the action of an external directional electric field (OEEF), the CP molecule wakes up the ionic structure in Fig. 5(a_1). Fig. 5(a_3) shows that in the absence of any obstacles, the molecules generally align their overall dipole moment with the direction of the electric field. In conclusion, OEEF also induces dipole orientations in molecules that are “rolling

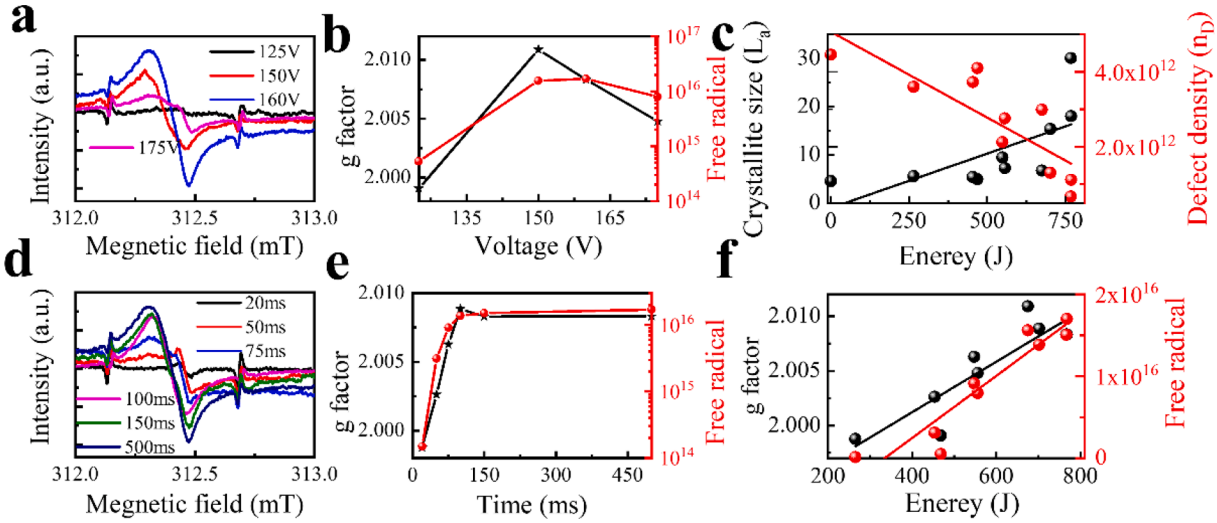


**Fig. 4.** EPR characterization of FG: (a) EPR signals obtained under different FJH voltages; (b) the Free radical concentration and g factor of EPR signals obtained under different FJH voltages; (c) crystallite size and defect density with input energy; (d) the EPR signal obtained under different FJH times; (e) the Free radical concentration and g factor of the EPR signal obtained under different FJH times; (g) g-factor and radical concentration with input energy.

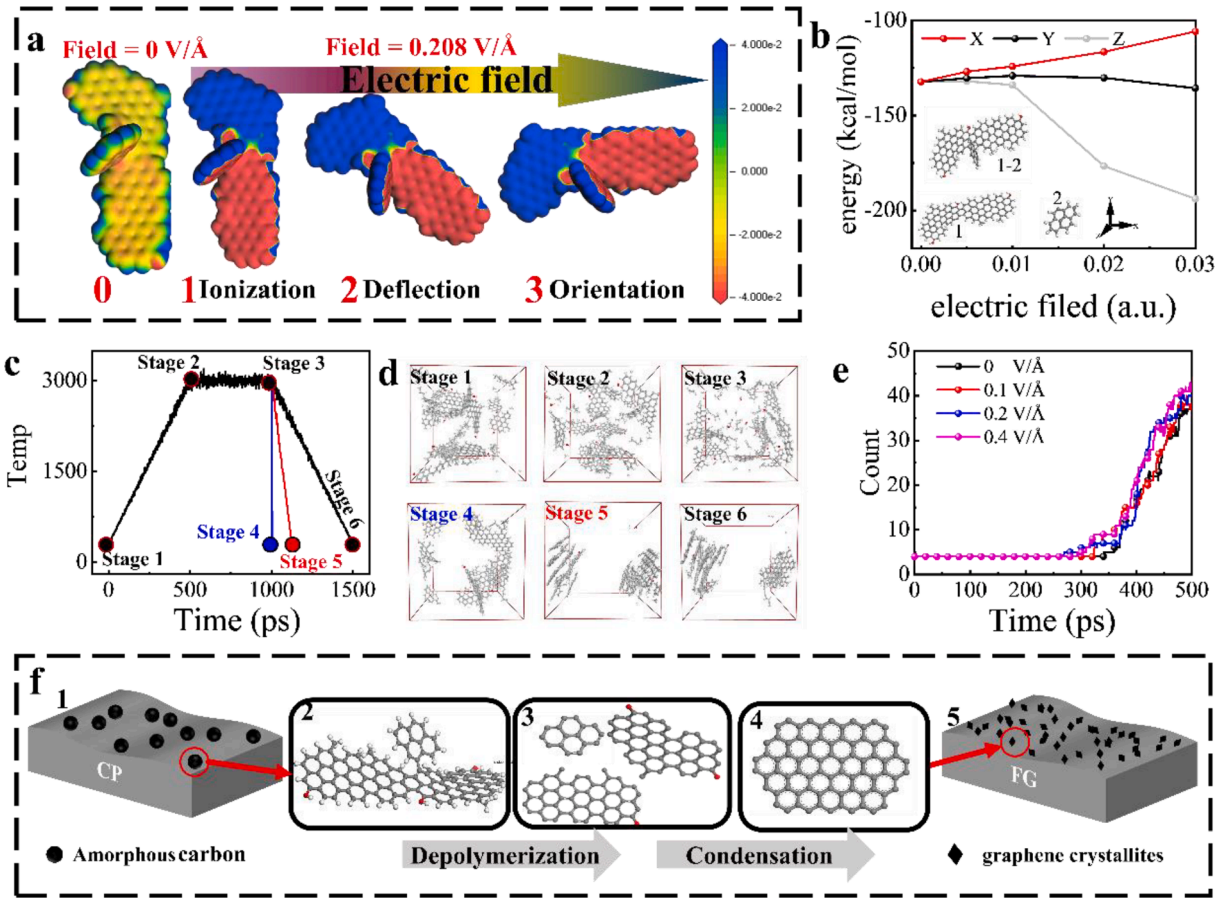


**Fig. 5.** (a) The motion of CP molecules under the action of electric field; (b) The effect of electric field direction and intensity on the dissociation of CP molecular bonds; (a) Motion of CP molecules under the action of electric field; (b) Effect of electric field direction and intensity on the dissociation of CP molecular bonds; (c) Temperature control curve of molecular dynamics; (d) Snapshots of molecular dynamics at different cooling rates; (e) Curves of molecular number with time during molecular dynamics under the action of different electric field intensities; (f) the schematic diagram of the mechanism of FG formation.

freely" (Fig. 5(a_2)). At the same time, reactions often exhibit an insurmountable reaction barrier making them "forbidden" in the absence of catalysts. However, with the help of OEEF, the electron recombination from reactant to product bonding occurs in the same direction as the electric field. This arrangement transfers electrons from the donor reactant to the acceptor in the direction of the OEEF. As a result, the reaction barrier is lowered by tens of kcal $mol^{-1}$, as shown in Fig. 5(b), applying an electric field in the X axis can lower the reaction energy barrier.

Molecular dynamics simulations were further carried out to demonstrate that its ultrafast cooling rate could make the resulting graphene microcrystalline turbolayers arranged and the electric field could induce the decomposition of CP molecules. First, the coal pitch molecules are heated from 300 K to 3000 K, as shown in Fig. 5(c). Under the action of high temperature, the branch chain of coal tar pitch is broken to generate vinyl radical, methyl radical and hydrogen radical, and these radicals have high reactivity. Some of them are grafted onto the graphene crystallites of CP molecules, and a small amount of the grafted carbon atoms form a graphene-like carbon ring with the original graphene carbon atoms, as shown in Fig. 5(d-3). Fig. 5(d) reflects the evolution of the atomic structure at different stages, where the cooling rates of stages 4–6 are 540, 54, and 5.4 K/ps, respectively. The rapid cooling makes the graphene crystallites too late for AB stacking to generate graphite. In addition, the initial decomposition temperature is also different under the action of different electric fields. Fig. 5(e) shows that the initial decomposition temperature decreases with the increase of the electric field, and the number of small molecules obtained by the decomposition is more, and the number of free radicals is also more. Therefore, FG is generated from CP under the joint coupling of external electric field and temperature field of FJH process.

More importantly, by using FJH to perform ultra-fast thermal decomposition of the carbon on the carbon support, graphite nanosheets can be synthesized in situ on the carbon substrate. In detail, Fig. 5(f) shows the formation process of FG. Firstly, the CP is mainly composed of a matrix of fused-ring aromatic hydrocarbon compounds and amorphous carbon crystallites (Fig. 5,(f-1)). At that time, the crystallites can be regarded as some large clusters of atoms, which, with a hexagonal and regularly arranged structure, have the basis for transforming into a graphite structure (Fig. 5(f-2)). Secondly, under the flash joule thermal shock, the side chains on the edge of the crystallites begin to break or vaporize, or enter the planar grid of carbon atoms, and undergo a series of reactions such as continuous decomposition and polymerization (Fig. 5(5–3)). Thirdly, the plane-oriented crystallites gradually combine into larger plane bodies at high temperature (Fig. 5(f-4)). Finally, when the crystallites gradually transform from the disorderly arrangement in the two-dimensional space to the ordered arrangement in the three-dimensional space, graphite nanosheets are finally formed (Fig. 5(f-5)). In short, during the 500 ms FJH process, due to the ultra-high temperature generated by thermal shock, the carbon source precursor continuously decomposes and polymerizes, and solidifies into nanosheets within milliseconds after cooling, thereby producing uniformly dispersed carbon nanosheets on the carbon carrier. This leads to the overall bottom-up synthesis of graphene as shown in Fig. 5(f).

In addition, the electrochemical characteristics of the produced coal-based graphene were verified from the EDLC-based supercapacitor. Fig. 6(a & b) shows the CV curve of a supercapacitor battery with coal-

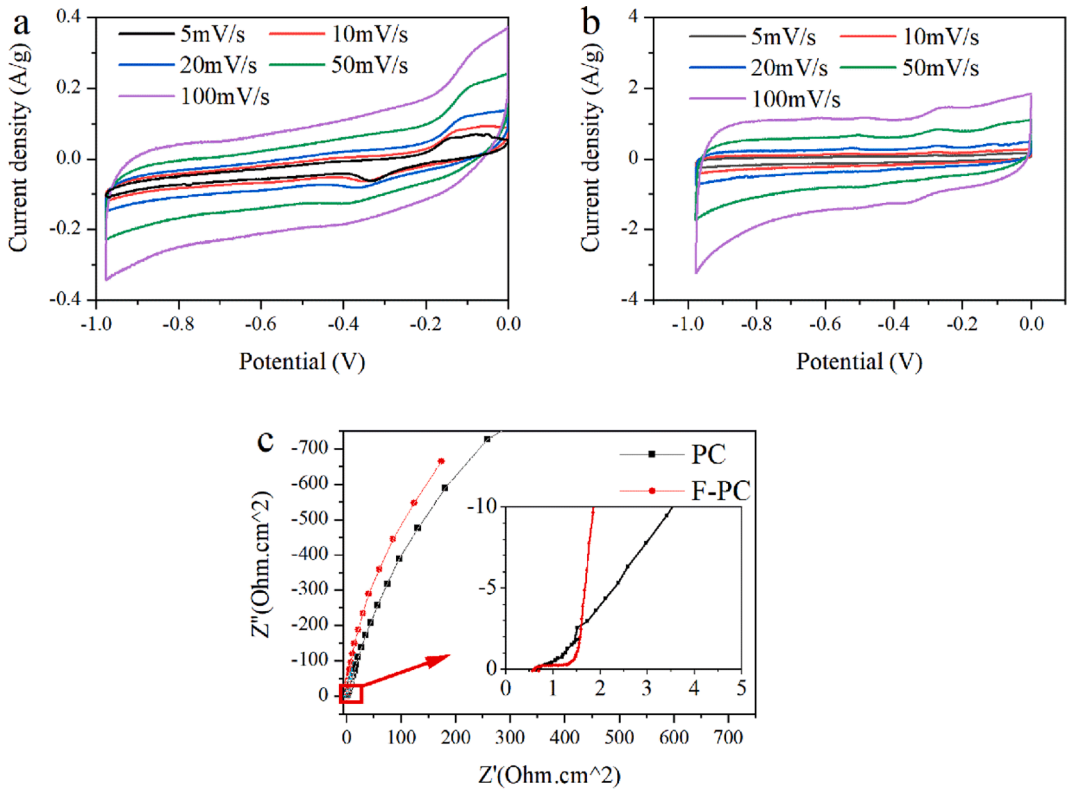


**Fig. 6.** (a-b) CV curves of CP and FG-160; (c) Nyquist plots of PC and FG-160.

based porous carbon electrodes. The flash-treated coal-based graphene shows a larger area in the CV curve, which denotes that it has the highest specific capacitance. After FJH treatment, it shows approximately rectangular characteristics without significant redox peaks, indicating that there is mainly an electric double layer on the electrode. In addition, the phenomenon that the CV curve deviates from the rectangle is due to the polarization of the electrode at a higher scanning speed. Fig. 6(c) is the Nyquist diagram of PC and FG, and the inset is an enlarged diagram of the high frequency region. In the low frequency region, the slope of F-PC is larger, indicating that FJH can improve the capacitance characteristics of PC.

## 4. Conclusion

In this study, the FJH system based on capacitor discharge was used to treat the coal pitch. The morphology, structure, and chemical composition of the coal pitch before and after the flash treatment were characterized. The results show that coal pitch is transformed into FG; and as the input energy increases, the defect density of the FG produced would decrease, and the size of the aromatic sheet increase. The FG produced displays good electronic information of two-dimensional graphene. The concentration of free radicals is also increased, which is mainly due to the disordered arrangement of the aromatic layers rather than internal defects. Finally, the mechanism of action of the FJH is explained in terms of the molecular dynamics of the reaction and DFT calculations, where Joule heat provides energy for the kinetics and thermodynamics of the reaction. The high temperature (3000 K) can dissociate the branched chains in CP and produce highly reactive alkane and olefin radicals, which provide carbon sources for graphene growth. Meanwhile, the faster cooling rate of FJH can generate disordered FG, which effectively prevents its graphene microcrystal AB stacking.

## CRediT authorship contribution statement

**Pengfei Huang:** Conceptualization, Methodology, Validation, Investigation, Writing – original draft, Funding acquisition, Project administration. **Rongtao Zhu:** Investigation, Validation, Writing – review & editing, Funding acquisition, Project administration. **Xinxi Zhang:** Conceptualization, Resources, Writing – review & editing, Supervision. **Wenjun Zhang:** Writing – review & editing, Supervision, Funding acquisition.

## Declaration of Competing Interest

The authors declare that they have no known competing financial interests or personal relationships that could have appeared to influence the work reported in this paper.

## Data availability

Data will be made available on request.

## Acknowledgements

This work was supported by Fundamental Research Funds for the Central Universities (China University of Mining and Technology) (2019GF08), National Natural Science Foundation of China (51974307), Key Research and Development Project of Xuzhou City (KC21287), the Assistance Program for Future Outstanding Talents of China University of Mining and Technology (2021WLJCRCZL038) and the Postgraduate Research & Practice Innovation Program of Jiangsu Province (KYCX21_2426).

## Appendix A. Supplementary data

Supplementary data to this article can be found online at https://doi.

org/10.1016/j.cej.2022.137999.

## References


[1] L. Lin, H. Peng, Z. Liu, Synthesis challenges for graphene industry, Nat. Mater 18 (6) (2019) 520–524, https://doi.org/10.1038/s41563-019-0341-4.

[2] I. Levchenko, K.K. Ostrikov, J. Zheng, X. Li, M. Keidar, K.B. Teo, Scalable graphene production: Perspectives and challenges of plasma applications, Nanoscale 8 (20) (2016) 10511–10527, https://doi.org/10.1039/C5NR06537B.

[3] R.C. Sinclair, J.L. Suter, P.V. Coveney, Micromechanical exfoliation of graphene on the atomistic scale, Phys. Chem. Chem. Phys 21 (10) (2019) 5716–5722, https://doi.org/10.1039/C8CP07796G.

[4] G. Salussolia, E. Barbieri, N.M. Pugno, L. Botto, Micromechanics of liquid-phase exfoliation of a layered 2D material: a hydrodynamic peeling model, J. Mech. Phys. Solids 134 (2020), 103764, https://doi.org/10.1016/j.jmps.2019.103764.

[5] R. Muzyka, S. Drewniak, T. Pustelny, M. Chrubasik, G. Gryglewicz, Characterization of graphite oxide and reduced graphene oxide obtained from different graphite precursors and oxidized by different methods using Raman spectroscopy, Materials 11 (7) (2018) 1050, https://doi.org/10.3390/ma11071050.

[6] C.P.P. Soares, R.d.L. Baptista, D.V. Cesar, Solvothermal reduction of graphite oxide using alcohols, Mater. Res 21 (1) (2017) e2017072.

[7] X. Wang, Q. Yuan, J. Li, F. Ding, The transition metal surface dependent methane decomposition in graphene chemical vapor deposition growth, Nanoscale 9 (32) (2017) 11584–11589, https://doi.org/10.1039/C7NR02743E.

[8] W. Yang, G. Chen, Z. Shi, C.-C. Liu, L. Zhang, G. Xie, M. Cheng, D. Wang, R. Yang, D. Shi, K. Watanabe, T. Taniguchi, Y. Yao, Y. Zhang, G. Zhang, Epitaxial growth of single-domain graphene on hexagonal boron nitride, Nat. Mater 12 (9) (2013) 792–797.

[9] K.A. Madurani, S. Suprapto, N.I. Machrita, S.L. Bahar, W. Illiya, F. Kurniawan, Progress in graphene synthesis and its application: history, challenge and the future outlook for research and industry, Ecs. J. Solid. State. Sc 9 (9) (2020), 093013, https://doi.org/10.1149/2162-8777/abbb6f.

[10] J. Qin, Y. Zhang, M. Batmunkh, G. Shi, M. Al-Mamun, P. Liu, W. Li, D.-C. Qi, H. Zhao, Y.L. Zhong, Fast and cost-effective room temperature synthesis of high quality graphene oxide with excellent structural intactness, Sustain. Mater. Techno 25 (2020) e00198.

[11] C. Zhu, S. Guo, P. Wang, L. Xing, Y. Fang, Y. Zhai, S. Dong, One-pot, water-phase approach to high-quality graphene/TiO 2 composite nanosheets, Chem. Commun 46 (38) (2010) 7148–7150, https://doi.org/10.1039/C0CC01459A.

[12] A. Jolly, D. Miao, M. Daigle, J.F. Morin, Emerging Bottom-Up Strategies for the Synthesis of Graphene Nanoribbons and Related Structures, Angew. Chem 132 (12) (2020) 4652–4661, https://doi.org/10.1002/ange.201906379.

[13] J. Kotakoski, A. Krasheninnikov, U. Kaiser, J. Meyer, From point defects in graphene to two-dimensional amorphous carbon, Phys. Rev. Lett 106 (10) (2011), 105505, https://doi.org/10.1103/PhysRevLett.106.105505.

[14] G.S. Bang, G.W. Shim, G.H. Shin, D.Y. Jung, H. Park, W.G. Hong, J. Choi, J. Lee, S.-Y. Choi, Pyridinic-N-doped graphene paper from perforated graphene oxide for efficient oxygen reduction, ACS. Omega 3 (5) (2018) 5522–5530, https://doi.org/10.1021/acsomega.8b00400.

[15] I.A. Baburin, A. Klechikov, G. Mercier, A. Talyzin, G. Seifert, Hydrogen adsorption by perforated graphene, Int. J. Hydrogen. Energ 40 (20) (2015) 6594–6599, https://doi.org/10.1016/j.ijhydene.2015.03.139.

[16] L. Jiang, T. Niu, X. Lu, H. Dong, W. Chen, Y. Liu, W. Hu, D. Zhu, Low-temperature, bottom-up synthesis of graphene via a radical-coupling reaction, J. Am. Chem. Soc 135 (24) (2013) 9050–9054, https://doi.org/10.1021/ja4031825.

[17] L. Huang, Q. Chang, G. Guo, Y. Liu, Y. Xie, T. Wang, B. Ling, H. Yang, Synthesis of high-quality graphene films on nickel foils by rapid thermal chemical vapor deposition, Carbon 50 (2) (2012) 551–556, https://doi.org/10.1016/j.carbon.2011.09.012.

[18] W.A. Algozeeb, P.E. Savas, D.X. Luong, W. Chen, C. Kittrell, M. Bhat, R. Shahsavari, J.M. Tour, Flash graphene from plastic waste, ACS. Nano 14 (11) (2020) 15595–15604, https://doi.org/10.1021/acsnano.0c06328.

[19] P.A. Advincula, D.X. Luong, W. Chen, S. Raghuraman, R. Shahsavari, J.M. Tour, Flash graphene from rubber waste, Carbon 178 (2021) 649–656, https://doi.org/10.1016/j.carbon.2021.03.020.

[20] D.X. Luong, K.V. Bets, W.A. Algozeeb, M.G. Stanford, C. Kittrell, W. Chen, R. V. Salvatierra, M. Ren, E.A. McHugh, P.A. Advincula, Z. Wang, M. Bhatt, H. Guo, V. Mancevski, R. Shahsavari, B.I. Yakobson, J.M. Tour, Gram-scale bottom-up flash graphene synthesis, Nature 577 (7792) (2020) 647–651.

[21] W. Chen, J.T. Li, Z. Wang, W.A. Algozeeb, D.X. Luong, C. Kittrell, E.A. McHugh, P. A. Advincula, K.M. Wyss, J.L. Beckham, M.G. Stanford, B.o. Jiang, J.M. Tour, Ultrafast and Controllable Phase Evolution by Flash Joule Heating, ACS. Nano 15 (7) (2021) 11158–11167.

[22] B. Deng, D.X. Luong, Z. Wang, C. Kittrell, E.A. McHugh, J.M. Tour, Urban mining by flash Joule heating, Nat. Commun 12 (1) (2021) 1–8, https://doi.org/10.1038/s41467-021-26038-9.

[23] M.G. Stanford, K.V. Bets, D.X. Luong, P.A. Advincula, W. Chen, J.T. Li, Z. Wang, E. A. McHugh, W.A. Algozeeb, B.I. Yakobson, J.M. Tour, Flash graphene morphologies, ACS. Nano 14 (10) (2020) 13691–13699.

[24] K.M. Wyss, J.L. Beckham, W. Chen, D.X. Luong, P. Hundi, S. Raghuraman, R. Shahsavari, J.M. Tour, Converting plastic waste pyrolysis ash into flash graphene, Carbon 174 (2021) 430–438, https://doi.org/10.1016/j.carbon.2020.12.063.

[25] K. Li, R. Khanna, H. Zhang, A. Conejo, S. Ma, Z. Liang, G. Li, M. Barati, J. Zhang, Thermal behaviour, kinetics and mechanisms of CO2 interactions with graphene: An atomic scale reactive molecular dynamic study, Chem. Eng. J 425 (2021), 131529, https://doi.org/10.1016/j.cej.2021.131529.

[26] J. Yuan, Y. Wen, D.D. Dionysiou, V.K. Sharma, X. Ma, Biochar as a novel carbon-negative electron source and mediator: electron exchange capacity (EEC) and environmentally persistent free radicals (EPFRs): a review, Chem. Eng. J 429 (2022), 132313, https://doi.org/10.1016/j.cej.2021.132313.

[27] Y. Mao, K.K. Gleason, Hot filament chemical vapor deposition of poly (glycidyl methacrylate) thin films using tert-butyl peroxide as an initiator, Langmuir 20 (6) (2004) 2484–2488, https://doi.org/10.1021/la0359427.

[28] G.B. Blanchet, Laser ablation and the unzipping of addition polymer, J. Aapp. Phys 80 (7) (1996) 4082–4089, https://doi.org/10.1063/1.363278.

[29] H. Yasuda, T. Hsu, Some aspects of plasma polymerization investigated by pulsed RF discharge, J. Polym. Sci. A. Polym. Chem 15 (1) (1977) 81–97, https://doi.org/10.1002/pol.1977.170150109.

[30] G. Vitiello, G. De Falco, F. Picca, M. Commodo, G. D'Errico, P. Minutolo, A. D'Anna, Role of radicals in carbon clustering and soot inception: A combined EPR and Raman spectroscopic study, Combust. Flame 205 (2019) 286–294, https://doi.org/10.1016/j.combustflame.2019.04.028.

[31] Y. Qin, G. Li, Y. Gao, L. Zhang, Y.S. Ok, T. An, Persistent free radicals in carbon-based materials on transformation of refractory organic contaminants (ROCs) in water: a critical review, Water. research 137 (2018) 130–143, https://doi.org/10.1016/j.watres.2018.03.012.

[32] P. Huang, R. Zhu, X. Zhang, W. Zhang, A milliseconds flash joule heating method for the regeneration of spent cathode carbon, J Environ Sci Heal A 57 (1) (2022) 33–44.

[33] R. Serrazina, P.M. Vilarinho, A.M. Senos, L. Pereira, I.M. Reaney, J.S. Dean, Modelling the particle contact influence on the Joule heating and temperature distribution during FLASH sintering, J. Eur. Ceram 40 (4) (2020) 1205–1211, https://doi.org/10.1016/j.jeurceramsoc.2019.12.015.

[34] B. Li, L. Zhou, D. Wu, H. Peng, K. Yan, Y. Zhou, Z. Liu, Photochemical chlorination of graphene, ACS. nano 5 (7) (2011) 5957–5961, https://doi.org/10.1021/nn201731t.

[35] T. Jawhari, A. Roid, J. Casado, Raman spectroscopic characterization of some commercially available carbon black materials, Carbon 33 (11) (1995) 1561–1565, https://doi.org/10.1016/0008-6223(95)00117-V.

[36] T. Chang, Q. Guo, H. Hao, B. Wu, Y. Yang, Formation of radicals in coal pyrolysis examined by electron spin resonance, AIP Advances 7 (9) (2017), 095303, https://doi.org/10.1063/1.4986270.